2	dependent valence electronic structure of Pt nanoparticles
3	David P. Dean ^a , Gaurav S. Deshmukh ^a , Christopher K. Russell ^a , Kuixin Zhu ^b , Christina W. Li ^b , Jeffrey P. Greeley ^a , Denis Leshchev ^{c,*} , Eli Stavitski ^{c,*} , Jeffrey T. Miller ^{a,*}
5	^a Davidson School of Chemical Engineering, Purdue University, West Lafayette, IN 47907, USA
6	^b Department of Chemistry, Purdue University, West Lafayette, IN 47907, USA
7	^c Brookhaven National Laboratory NSLS-II, Upton, NY 11973, USA
8	
9	*Corresponding authors:
10	jeffrey-t-miller@purdue.edu
11	dleschev@bnl.gov
12	<u>istavitski@bnl.gov</u>
13	
14	
15	
16	
17	
18	
19	
20	
21	
22	
23	
24	
25	
26	
27	
28	Abstract

X-ray characterization of catalyst materials using synchrotron radiation has become more widely available to the scientific community in recent decades. Techniques such as X-ray absorption spectroscopy (XAS) and resonant inelastic X-ray scattering (RIXS) have enabled insitu and in-operando studies of dilute catalyst sites for heterogeneous catalyst materials in order to obtain information about local geometric and electronic structure and how it impacts chemical transformations. Non-resonant or valence-to-core X-ray emission spectroscopy (NR-XES or VtC-XES) is an emerging technique used to probe changes to the d-electron density of states (d-DOS) for various factors such as ligand environment or alloy formation. In this study, VtC-XES provides insights into the electronic structure of Pt nanoparticles of different sizes dispersed in a typical heterogeneous catalyst support of SiO₂. The results experimentally verify that the d-band center of the Pt catalysts systematically increases with decreasing nanoparticle size. Going from a fullycoordinated Pt foil to Pt nanoparticles of 2 nm in diameter, the shift in the d-band center scales linearly with the proportion of surface Pt atoms to bulk Pt atoms. While VtC-XES shows that the filled Pt 5d states shift systematically to higher energy, XANES shows that the unfilled Pt 5d states also shift systematically to higher energy. These findings align with previous computational and experimental studies, and confirm that in-situ VtC-XES is a capable technique for assessing the d-DOS of catalyst materials. Moreover, an XAS beamline can assess multiple aspects of both the geometric and electronic structure of a catalyst. A more precise determination of electronic structure can be correlated with heats of adsorption of various adsorbates in order to drive the design of future catalyst materials.

49

29

30

31

32

33

34

35

36

37

38

39

40

41

42

43

44

45

46

47

48

51

50

52

53

54

55

56

57

Keywords: X-ray emission spectroscopy, Platinum catalyst, d-band center, nanoparticle size.

1. Introduction

The ability to characterize catalysts at the atomic level is critical to accelerated discovery and development of new materials. Significant improvements in characterization techniques such as synchrotron X-ray absorption spectroscopy (XAS), including improved synchrotron design and detector technology as well as accessibility, have enabled analyses such as X-ray absorption near edge structure (XANES) and extended X-ray absorption fine structure (EXAFS) for characterization of active sites in metal catalysts. ANES provides useful information about the electronic structure and is often used to obtain oxidation states. EXAFS yields information about bond distances and local coordination, including the number and types of atoms.

58

59

60

61

62

63

64

65

66

67

68

69

70

71

72

73

74

75

76

77

78

79

80

81

82

83

84

85

86

87

The future of catalyst material discovery is expected to mirror future developments in characterization methods. Resonant inelastic X-ray scattering (RIXS) has been recently developed to assess the electronic structure of metallic catalyst materials.^{6,7} RIXS is a two-step process involving a resonant excitation of a core electron into an intermediate state and a subsequent decay into a final state, emitting an X-ray. Within the past two decades, RIXS has been used for in-situ metallic catalyst studies to determine the structure of the valence electron band.^{5,22} More recently, the method has been extended to 5d metal catalysts such as Pt and Ir to obtain electronic information about the average energy of filled and unfilled 5d valence states. 5,14,15,23-25 Despite the technique development, information about the entire filled density of states of 5d metal materials remains elusive. Using RIXS, the different intermediate states can interfere with one another because of the large number of resonant states.²² RIXS can circumvent core-hole lifetime broadening to achieve high energy resolution but is susceptible to considerable uncertainty incurred when subtracting the elastic scattering line from the spectra. 14,22,48 This implies that only the average energy of the filled valence states can be ascertained. Valence-band X-ray or ultraviolet photoelectron spectroscopy (VB – XPS or UPS) experiments have been successfully used to determine the d-electron density of states (d-DOS) distribution for metals. 18,20,26,33 Nevertheless, the photoemission of valence electrons is limited to a soft X-ray range, which requires ultra-high vacuum. This is not compatible with *in-situ* applications where the emitted Xrays must have sufficient energy to penetrate reacting gases, catalyst particles, cell windows, etc. This makes it difficult to discern whether an electronic change can be attributed to differences in surface adsorbates or a property inherent to the bulk material (e.g. surface oxidation of a nanoparticle or the formation of an alloy). Additionally, the subtraction of the background or the deconvolution of contributions of other elements in the sample may introduce significant uncertainty. 20,34

Non-resonant X-ray emission spectroscopy (NR-XES), which focuses on the valence-tocore region (VtC-XES or V2C-XES), is an emerging technique that can probe the full distribution of the density of states while using hard X-rays, which affords element-specific analysis.⁵ Given the highly penetrative power of hard X-rays, VtC-XES is better suited for *in-situ* experiments which maintain the desired chemical environment (i.e. partial pressure of gases, temperature, pretreatment). 28 Additionally, the setup can be used in tandem with XAS analysis to provide a holistic picture of the geometric and electronic properties of a material. VtC-XES can decouple elastic and inelastic contributions to the X-ray emission by using an incident X-ray energy higher than that of the edge being studied, thereby exciting an electron into the continuum.⁵ Doing so turns the resulting decay of an electron to the core hole into a one-electron process whose specific energy can be selected using a crystal analyzer.²⁸ VtC-XES has historically been applied to 3d or 4d compounds with a high weight loading of the desired metal, such as Mn, Fe, Cr, Cu, or Nb in order to probe the electronic structure with a different ligand environment. ^{27,29,31,35,42} Due to recent improvements in synchrotron flux such as the development of 4th generation synchrotrons as well as the improvement of X-ray detector technology, VtC-XES has been extended to more dilute (~1 to 2 wt%) catalysts with 3d metals, such as Cu/SSZ-13, Fe/ZSM-5, or Pt/CeO_x (probing the Ce 3d states). 30,32,36 The technique has proven to be useful for in-situ and in-operando studies to probe changes under reaction conditions.^{7,32}

Nevertheless, there is significant opportunity for improvement of the VtC-XES technique. For example, there has been little application to 5d metals that are important catalyst materials such as Pt, Ir, or Au. This is in large part due to technological limitations for detecting the relatively weak Lβ₅ emission line, which represents a 5d_{5/2} or 5d_{3/2} to 2p_{3/2} transition.³⁹ This study focuses on Pt, which is widely used for important catalytic reactions in thermochemistry and electrochemistry such as alkane dehydrogenation or the electrochemical oxygen reduction reaction.^{37,38} VtC-XES affords the ability to obtain the structure of the Pt 5d-DOS for the filled states, while XANES affords information about the average energy of the Pt 5d unfilled states.³⁹ Very few studies have attempted VtC-XES on Pt catalyst materials. One such study resolves VtC-XES to apply to Pt and Au compounds in order to study the electronic structure of the 5d metal with different ligands.^{12,43} Another recent study extends XES to Pt-Ni nanoparticles, but instead

employs resonant X-ray emission spectroscopy (RXES), making it difficult to decouple resonant and non-resonant effects.^{34,41} Yet another study uses XES to explore Pt layers on a separate metal substrate, including alloys, but probes the oxygen K edge XES rather than Pt XES.⁴⁴

Herein, VtC-XES is employed to investigate the 5d-DOS for Pt nanoparticles supported on SiO₂ of various sizes similar to those commonly used as catalysts. Pt nanoparticles ranging from 2 to 5 nm are synthesized and characterized using STEM to confirm nanoparticle size. XAS and VtC-XES are employed to experimentally measure the average energy of the Pt filled and unfilled states, respectively. In this work, VtC-XES spectra were obtained for Pt nanoparticle samples of different sizes under *in-situ* reducing conditions in order to assess changes in the d-DOS such as d-band center, d-band width, etc. The experimentally determined impact of Pt nanoparticle size on the 5d-DOS is shown to shift the DOS to higher energy with decreasing size. Density functional theory (DFT) calculations performed on slabs and clusters in this study show an analogous shift with respect to undercoordinated Pt sites, which aligns with previous literature results.^{20,21}

2. Experimental Methods

2.1 Materials and Synthesis

Monometallic Pt nanoparticles of varying sizes on SiO₂ supports were synthesized via incipient wetness impregnation (IWI). Three monometallic Pt samples were synthesized (shorthand names are given in parentheses): 2 wt% Pt/SiO₂ (small), 2 wt% Pt/SiO₂ (medium), and 10 wt% Pt/SiO₂ (large) samples. In a typical synthesis, a tetraammineplatinum(II) nitrate [Pt(NH₃)₄(NO₃)₂, Sigma-Aldrich] is dissolved in ultrapure, deionized water to achieve a metal loading of 2 wt% or 10 wt%; 2 wt% was employed to achieve small and medium sized nanoparticles, while 10 wt% was used to make larger nanoparticles. The pH is adjusted to 11 using a minimal amount of 30% ammonium hydroxide solution [NH₄OH, Thermo Fisher Scientific]. The solution is then added dropwise onto Davisil® Grade 646 [35-60 mesh, pore size 150 Å, Sigma Aldrich] silica gel support. The material is dried at 120 °C for 12 hours and then calcined in air for 3 hours. The small sample was calcined at 225 °C, the medium sample at 300 °C, and the large sample at 450 °C. Subsequently, each sample is reduced in dilute hydrogen [5% H₂/He, Indiana Oxygen] for two hours. The small sample was reduced at 225 °C, the medium sample at 400 °C,

and the large sample at 550 °C. The goal to synthesize common Pt catalyst materials with a dilute Pt content (\sim 2 wt%).

A separate sample of Pt nanoparticles supported on silica was synthesized to serve as a standard reference to ensure energy calibration of the beamline setup. This sample was prepared similarly to the other samples with a weight loading of 3 wt% Pt, a calcination temperature of 250 °C, and a reduction temperature of 550 °C.

2.2 Scanning Transmission Electron Microscopy (STEM) Characterization

For scanning transmission electron microscopy (STEM), samples were prepared by drop-drying $10~\mu L$ of a 1 mg/mL supported catalyst suspension onto a Cu grid. High-angle annular dark-field scanning transmission electron microscopy (HAADF-STEM) were collected on an FEI Talos F200X S/TEM with a 200 kV X-FEG field-emission source.

Nanoparticle size was assessed using ImageJ software. Assuming spherical nanoparticles, the percentage of surface atoms was calculated for each nanoparticle using a ratio of the volume of a shell with a thickness of δ to the total volume of the sphere, given in Equation 1. The thickness of the shell was estimated to be equal to the Pt-Pt bond distance obtained using XAS, which is analogous to the atomic diameter of Pt, and d is the nanoparticle diameter. Overall dispersion was estimated by dividing the total number of surface atoms by the total number of atoms across all the nanoparticles considered.

$$\frac{V_{shell}}{V_{sphere}} = 1 - \left(\frac{d - 2\delta}{d}\right)^3 \tag{1}$$

2.3 X-ray Absorption Spectroscopy (XAS) Characterization

The XAS and XES measurements were conducted at the NSLS-II 8-ID Inner Shell Spectroscopy (ISS) beamline.³ XAS was conducted at the Pt L_{III} (11.564 keV) edge in transmission mode to obtain XANES and EXAFS. Three ion chambers were used for simultaneous measurement of a Pt foil energy calibration standard. The Pt foil is also used as a bulk metal (CN=12) Pt standard. Other Pt standards were diluted in boron nitride [BN, Thermo Fisher Scientific], ground into a fine powder, and pressed into wafers for *ex-situ* scans in transmission

mode. The Pt nanoparticle samples were inserted in capillaries, supported by a bed of quartz wool, and placed in an *in-situ* cell for gas and temperature treatment. The Pt nanoparticle samples were scanned in fluorescence mode using a Passivated Implanted Planar Silicon (PIPS) detector placed at a 45° angle from the incident beam. The PIPS detector was equipped with a gallium oxide (Ga₂O₃) filter in order to filter out elastic scattering. The *in-situ* cell is positioned to enable simultaneous fluorescence measurement of the sample as well as transmission measurement of the foil reference. In the *in-situ* cell, the Pt nanoparticle samples were pre-treated at 250 °C in 10% H₂ (balance He) for 30 minutes in order to remove surface oxygen from the nanoparticles, rendering them completely metallic. The sample was then cooled to 25 °C in He and scanned.

All spectra were analyzed using WinXAS 4.0 software.⁴ The XANES of the Pt compounds was used for analysis of oxidation state. Standard EXAFS fitting procedures were applied to the Pt nanoparticle samples in order to estimate Pt coordination and bond distances. A Pt-Pt scattering path was generated using the Pt foil as a fully coordinated (CN=12) metallic reference. Coordination number and % dispersion for Pt nanoparticles can be correlated by using the empirical relationship given in Equation 2 where *D* is percent dispersion.¹⁰

$$\log(D) = -0.13 \cdot CN_{Pt-Pt} + 2.58 \tag{2}$$

2.4 Valence-to-Core X-ray Emission Spectroscopy (VtC-XES) Characterization

The *in-situ* reactor is positioned such that simultaneous transmission, emission, and fluorescence are achievable. The incident X-ray energy was held at a constant value of 11900 eV, well above the edge energy of Pt L_{III}, thus constituting non-resonant X-ray emission spectroscopy. The spectrometer is a Johann spectrometer, equipped with a Si (933) spherically-bent crystal analyzer (SBCA) with a radius of curvature of 0.5 m. The crystal analyzer diffracts the emitted X-rays to a Detris Pilatus© detector positioned above the sample that moves in conjunction with the crystals, allowing the selection of a single emission energy that is focused to a single point on the detector. The crystal and detector move in a highly coordinated manner following a Rowland circle geometry.^{5,28} Energy resolution of the setup was estimated to be 1.9 eV using inelastic scattering. Between 10 and 20 VtC-XES scans were averaged for each sample. The d-band center is calculated by dividing the weighted average energy of the density of states distribution by the total number of d-band electrons. Mathematically, this is represented in Equation 3.¹⁶

$$\frac{\int \rho E dE}{\int \rho dE} \tag{3}$$

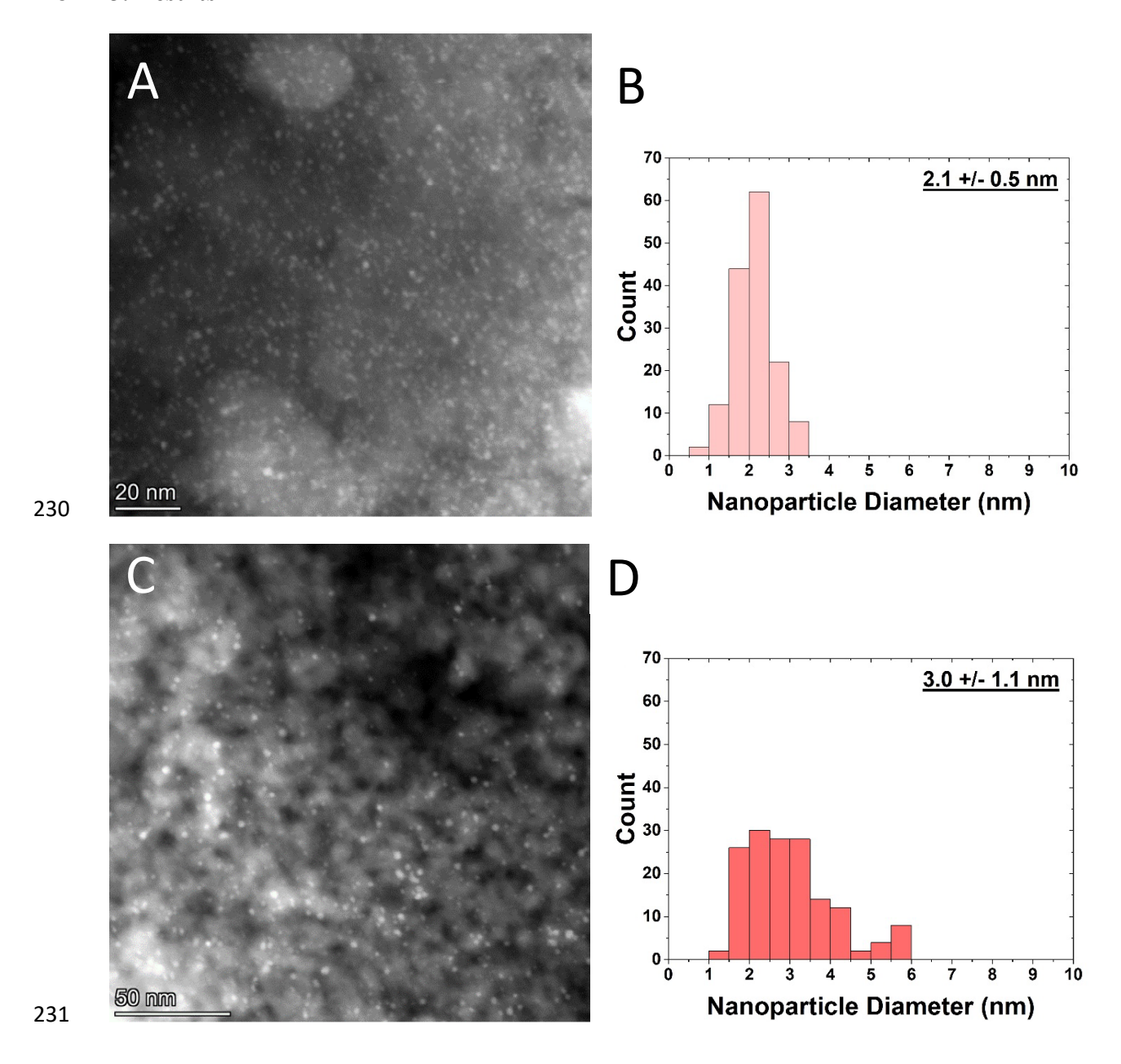
2.5 Density Functional Theory (DFT) Calculations

Pt nanoparticles were pre-relaxed using the effective medium theory (EMT) potential as implemented in the Python Atomic Simulation Environment (ASE).⁵⁰ Geometry relaxations were performed on pre-relaxed nanoparticles using plane-wave density functional theory (DFT) calculations as implemented in the Vienna Ab-initio Simulation Package (VASP) code⁵¹ with an energy cutoff of 400 eV and a single k-point. Relaxation was terminated when the Hellman-Feynman forces were below 0.02 eV/Å. Vacuum space of 40 Å was added in the unit cell to prevent interaction between periodic images. Single-point energy calculations with an energy cutoff of 600 eV were performed on converged geometries. Electron states above the Fermi level were populated above 0 K using Gaussian smearing. Core-electron states were modeled using the frozen core approximation and expressed using the Projector Augmented Wave (PAW) method.⁵² Projected density of states (pDOS) were calculated for Pt atoms in a range of -10 eV to 5 eV referenced to the Fermi level with an energy resolution of 0.0065 eV. pDOS spectra were smoothed using the Hanning window as implemented in Scipy⁵³ for visualization.

The d-band center was evaluated computationally as the first moment of the pDOS (Equation 4) where $E_{LB} = -10 \ eV$, $E_{UB} = 5 \ eV$, and $\rho(E - E_f)$ is the pDOS. The integrals were evaluated numerically using the trapezoidal method.

222
$$\epsilon_{d} = \frac{\int_{E_{LB}}^{E_{UB}} (E - E_{f}) \rho(E - E_{f}) d(E - E_{f})}{\int_{E_{LB}}^{E_{UB}} \rho(E - E_{f}) d(E - E_{f})}$$
(4)

3. Results



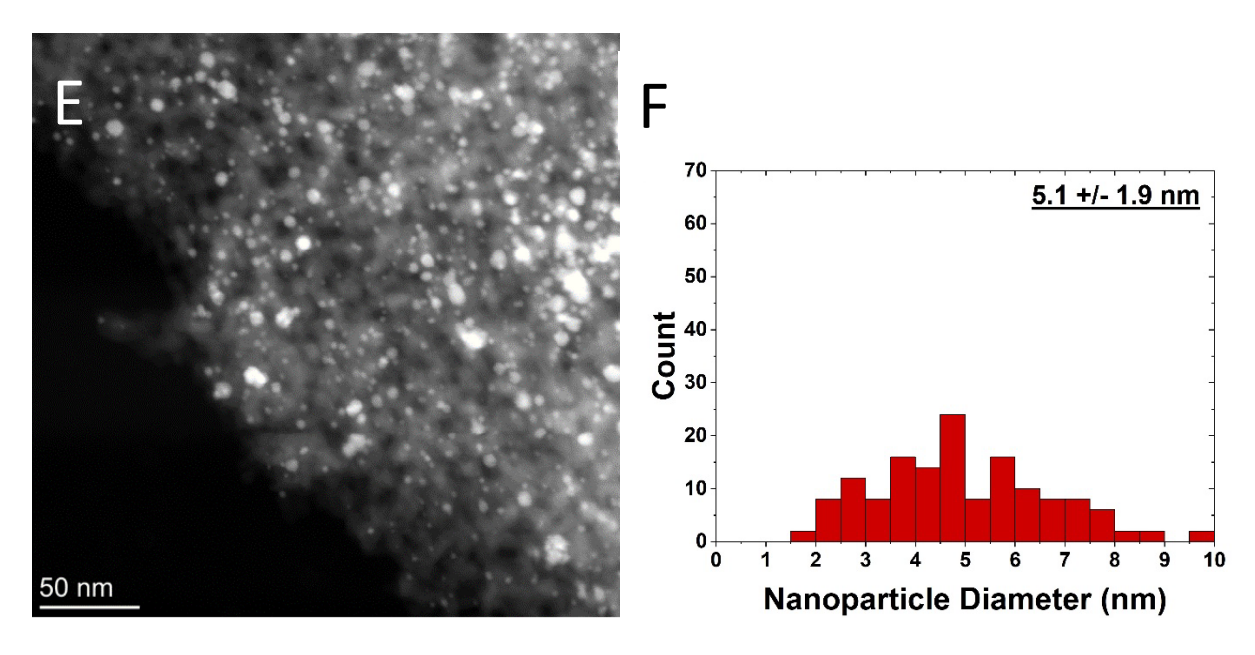


Figure 1. HAADF-STEM images and their corresponding size distributions of A,B) small Pt nanoparticle sample, C,D) medium Pt nanoparticle sample, and E,F) large Pt nanoparticle sample.

Nanoparticle size distributions were determined using HAADF-STEM (Figure 1). The small, medium, and large samples have an average diameter of 2.1 ± 0.5 nm, 3.0 ± 1.1 nm, and 5.1 ± 1.1 nm respectively. From these nanoparticle size distributions, dispersion was calculated based on an estimation of the total number of surface atoms relative to total nanoparticle volume, which increases with decreasing nanoparticle size, as shown in Table 1.

Table 1. Nanoparticle size and dispersion.

Sample	Nanoparticle Diameter (nm)	Dispersion (%)	
Pt foil	-	0	
Large Pt NPs	5.1 ± 1.9	23	
Medium Pt NPs	3.0 ± 1.1	37	
Small Pt NPs	2.1 ± 0.5	54	

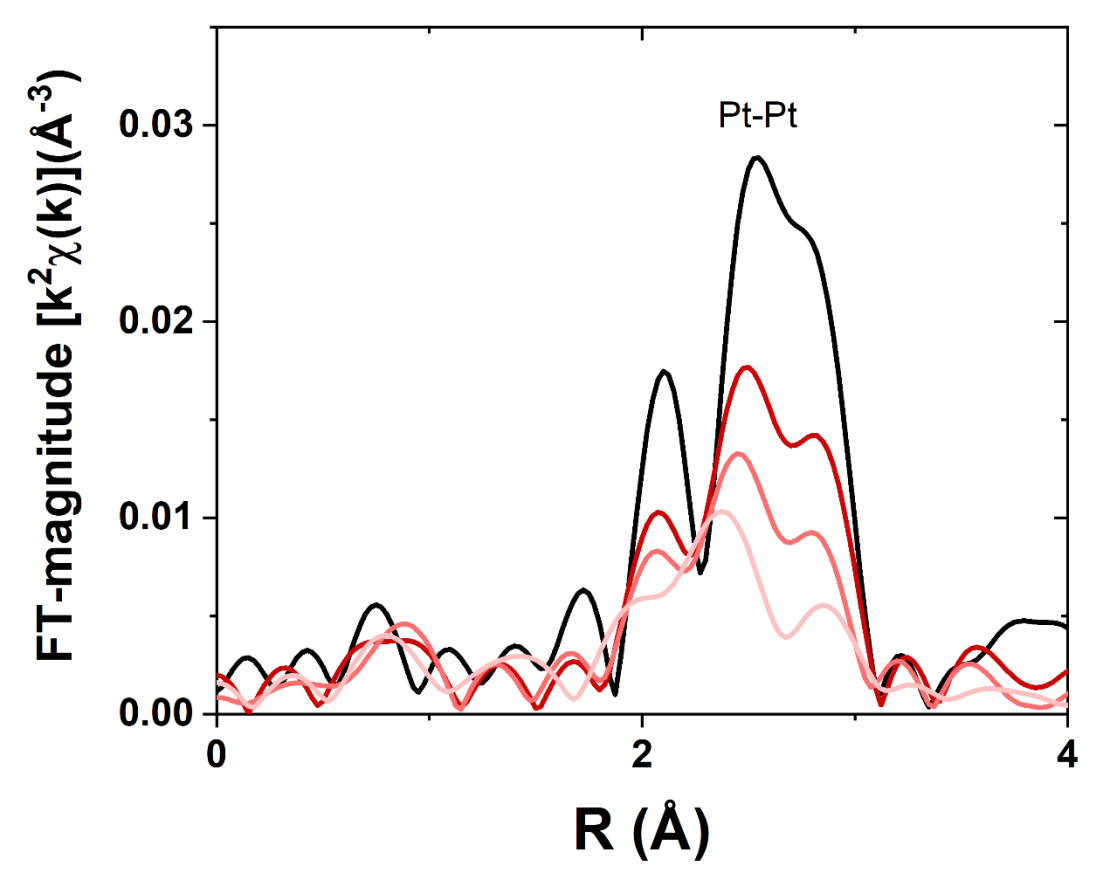


Figure 2. Pt L_{III} EXAFS for samples with Pt nanoparticles of different sizes. Pt foil (black), large sample (dark red), medium sample (moderate red), and small sample (light red).

To corroborate the nanoparticle size distribution as determined by STEM, EXAFS is also employed to determine nanoparticle dispersion. Three different Pt nanoparticle samples were reduced in H₂ at 250 °C to ensure no surface PtO is present. Subsequently, the samples were cooled to room temperature and scanned in flowing H₂. The three-peak pattern for all the samples is indicative of metallic Pt (Figure 2). There is no evidence of Pt-O scattering, which would occur at values of ~1.7 Å (phase-uncorrected distance), meaning that all Pt in the samples has been reduced by the pre-treatment in dilute H₂ at 250 °C. There is a systematic decrease in Fourier-transform magnitude with decreasing nanoparticle size, indicating a decrease in bulk average coordination. Additionally, the peaks shift to lower R with decreasing nanoparticle size, indicating bond contraction which is consistent with previous studies.^{8,10} The bond distance is assessed in the

EXAFS fitting results, which are given in Table 2. The value of S_o^2 , the amplitude reduction factor, was determined to be 0.81 based on the Pt foil reference. Using the phase and amplitude of an experimentally generated Pt-Pt scattering path from the Pt foil, the samples were found to have lower bulk-average Pt-Pt coordination relative to the foil. This is indicative of a higher proportion of undercoordinated Pt atoms to fully coordinated Pt atoms, meaning the nanoparticles are smaller with a lower Pt-Pt coordination.

Table 2. Pt L₃ edge XANES edge energy and EXAFS fits for the Pt foil and the small, medium, and large Pt nanoparticle samples.

Sample	Edge energy (keV)	Scattering Pair	CN (±10%)	R (±0.02 Å)	Δ σ ² (Å ²)	Shift in E _o (eV)
Pt foil	11.5644	Pt-Pt	12.0	2.77	0.004	7.0
Large Pt NPs	11.5646	Pt-Pt	10.1	2.76	0.006	-0.6
Medium Pt NPs	11.5648	Pt-Pt	8.3	2.74	0.007	-1.5
Small Pt NPs	11.5650	Pt-Pt	7.1	2.72	0.008	-2.1

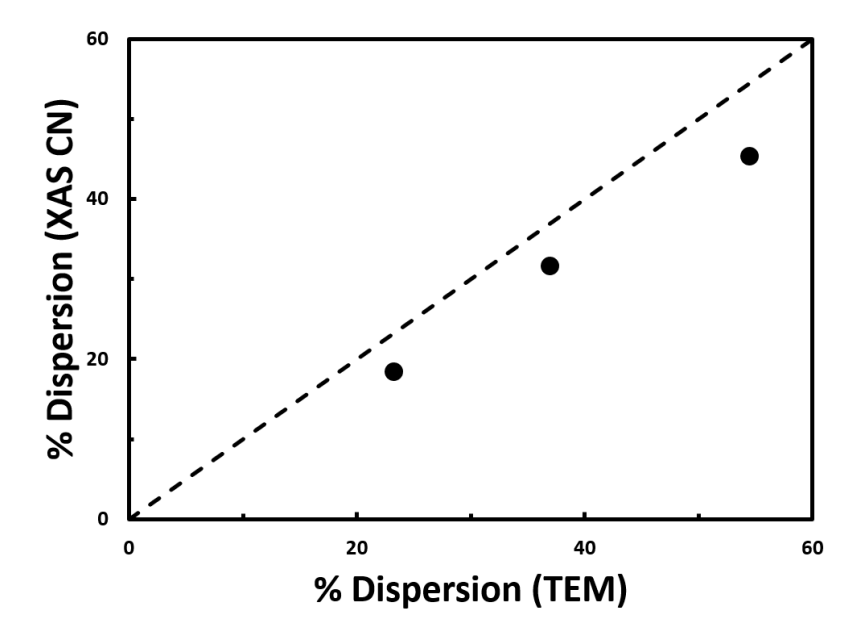


Figure 3. Dispersion determined from coordination number from EXAFS fitting versus dispersion determined from STEM. Results from the nanoparticle materials from this study (black circles) are plotted alongside the empirical relationship from literature (dashed black line). ¹⁰

The coordination number for Pt has been shown to be correlated with nanoparticle dispersion; thus, the nanoparticle dispersion can be independently calculated to corroborate the STEM results (Table 1). Nanoparticle dispersion calculated from XAS is consistent with the dispersion calculated from STEM (Figure 3).

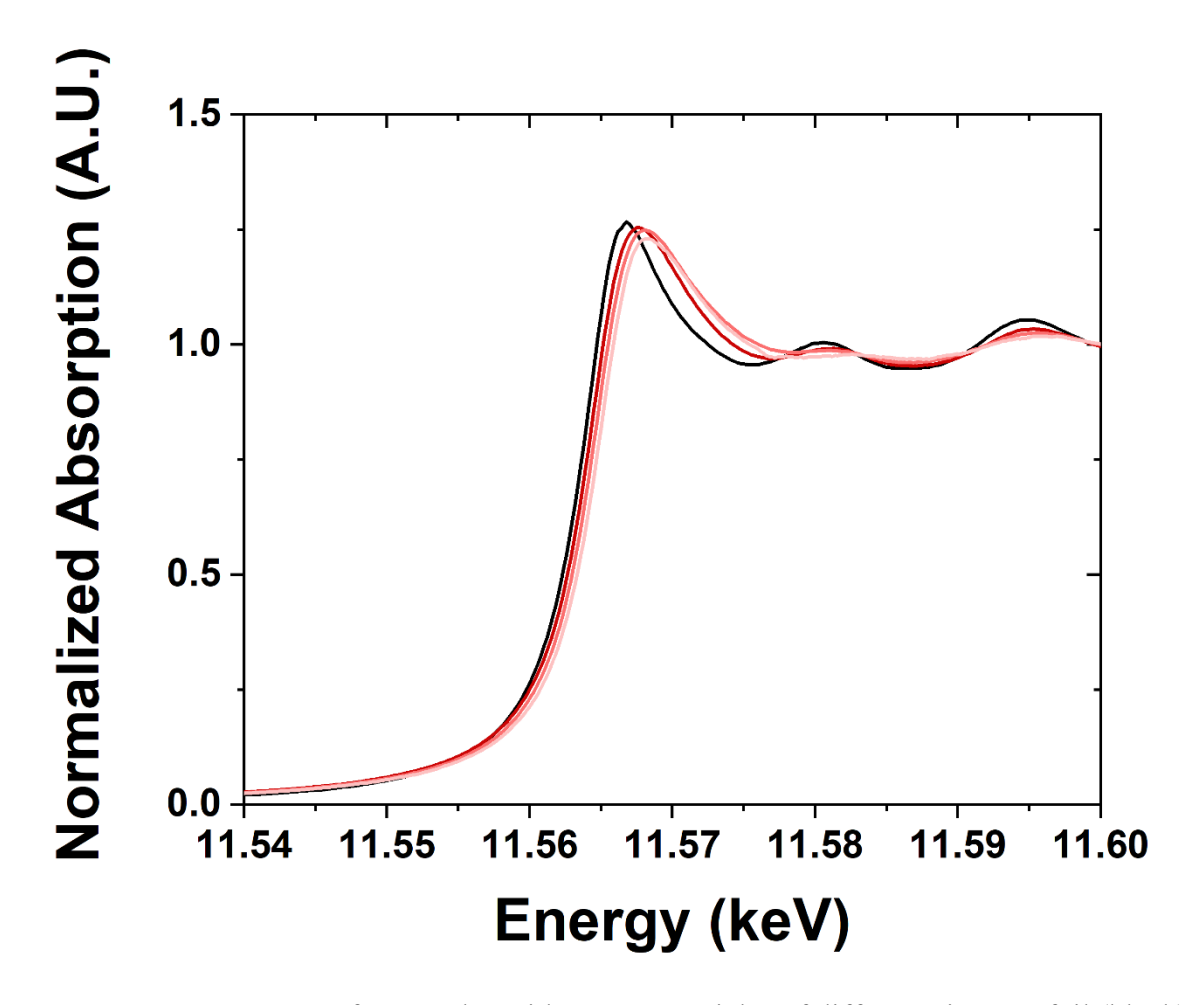


Figure 4. Pt L_{III} XANES for samples with Pt nanoparticles of different sizes. Pt foil (black), large sample (dark red), medium sample (moderate red), and small sample (light red).

The XANES for the samples (Figure 4) show a systematic increase in edge energy between 0.2 to 0.6 eV with decreasing nanoparticle size relative to the foil (Table 2), which is defined as the inflection point of the leading edge of the XANES spectrum.

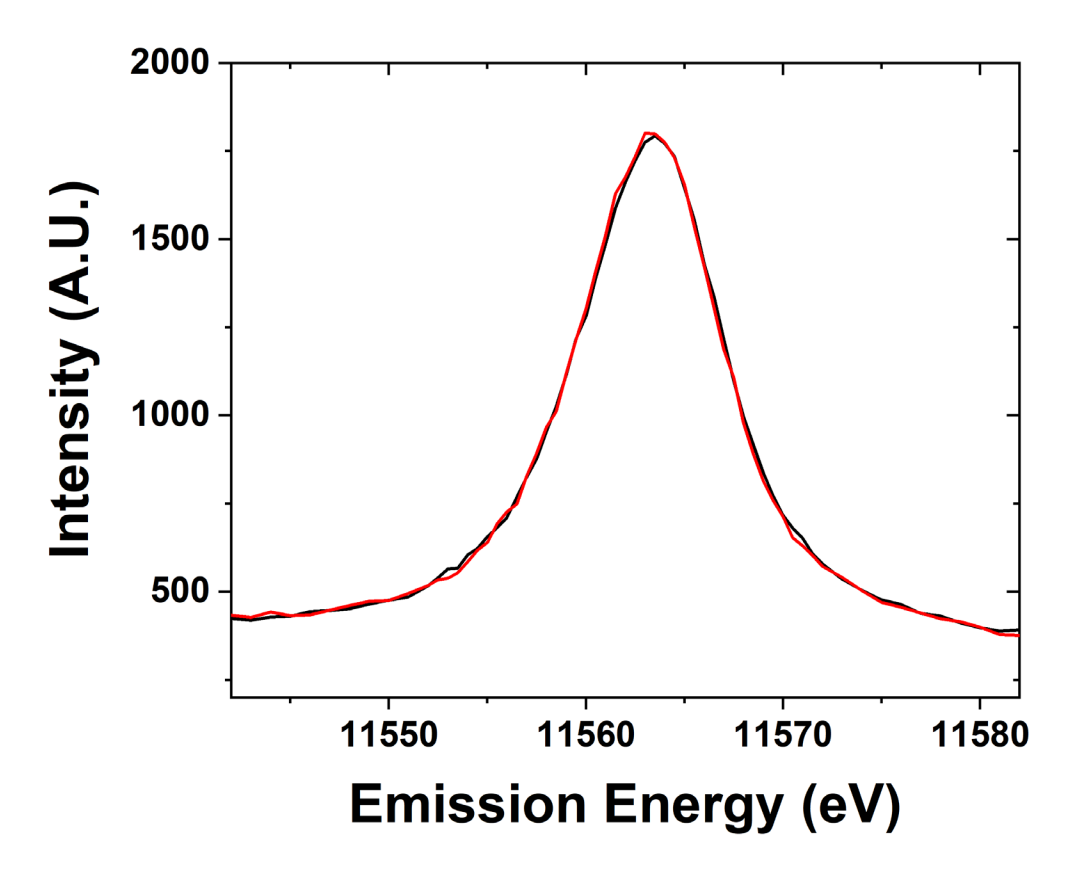


Figure 5. Day #1 (black) and Day #3 (red) VtC-XES calibration spectra.

The standard Pt catalyst reference sample was scanned periodically throughout the experiment, without gas or temperature treatment, to ensure the energy calibration of the beamline setup (Figure 5). The spectra for this sample are identical within +/- 0.1 eV. The spectra were normalized using the peak maximum and the baseline. The peaks are slightly skewed toward having a higher density at a higher energy level.

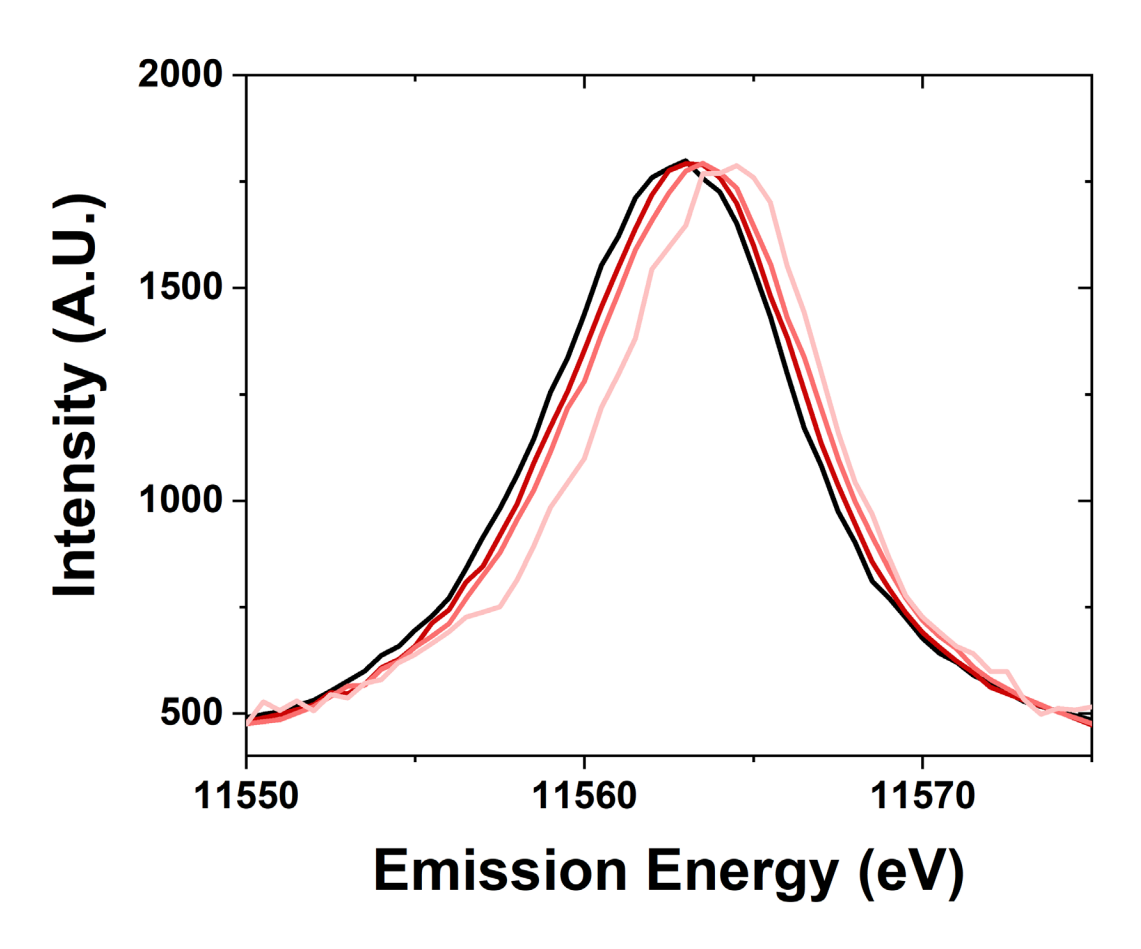


Figure 6. VtC-XES spectra for samples with Pt nanoparticles of different sizes. Pt foil (black), large sample (dark red), medium sample (moderate red), and small sample (light red).

The X-ray emission spectroscopy setup at the 8-ID beamline at the NSLS-II has the capability to detect the L β_5 VtC-XES spectra for 5d nano-materials and Pt foil (Figure 6). The Pt nanoparticle samples were scanned for VtC-XES after being reduced in H₂ at 250 °C. The VtC-XES spectra show a systematic increase in emission energy with decreasing nanoparticle size. The spectrum is analogous to a density of states (5d-DOS) distribution, and occurs at a similar energy (~11565 eV) compared to previous study of Pt compounds. ¹² In this case, the VtC-XES features at higher energy are closer to the Fermi level. Two metrics have been previously employed to assess the spectra: the d-band center and the full width at half maximum. The d-band center is defined as the first moment of the area underneath the distribution (relative to the baseline). ¹⁶ The full width at half maximum (FWHM, relative to baseline) intensity is a measure of the broadness

of the spectra. However, as evidenced by the shift to higher energy levels for the smaller nanoparticles (Figure 6), the spectra become increasingly shifted towards the Fermi level for smaller nanoparticles (i.e., shifted to higher energies). Thus, a third term to describe VtC-XES spectra is helpful for describing these energy shifts: the leading-edge energy. The proposed definition of the leading-edge energy is the energy of the right edge, or leading edge, of the spectrum at half maximum intensity, which is an estimate of the energy of the highest occupied molecular orbital (HOMO).

Table 3. Leading edge energy and d-band center energy for VtC-XES spectra of Pt nanoparticles.

Sample	Leading Edge Energy (eV)	d-band Center Energy (eV)	FWHM (eV)	XANES Edge energy (eV)
Pt foil	11566.6	11562.5	8.0	11564.4
Large Pt NPs	11567.0	11562.8	8.2	11564.6
Medium Pt NPs	11567.3	11563.1	8.0	11564.8
Small Pt NPs	11567.6	11563.6	7.4	11565.0

The metrics for VtC-XES are listed in Table 3 along with the XANES edge energy determined from XAS. The FWHM of the small sample has a slightly narrower XES spectrum compared to the other samples, which has been observed computationally for the d-DOS of small Pt nanoparticles.²¹ The FWHM metric value of ~7 to 8 eV is similar compared to computational predictions for the 5d-DOS of Pt.^{13,15,17} Additionally, it is similar compared to experimental predictions using XPS.^{18,20} Nonetheless, the spectra have a width of approximately 15 eV, which is double the width of computational or VB-XPS results for a Pt d-DOS and therefore merits discussion.

To probe the effect of changing nanoparticle size on the electronic structure and, specifically, the d-band center of Pt, density functional theory (DFT) calculations are performed on four octahedral nanoparticle clusters—Pt-38, Pt-79, Pt-201, and Pt-314 (Figure 7a-d, where the number indicates the number of atoms in the cluster). These correspond to nanoparticles with sizes

ranging from 0.8 nm–2.0 nm. While these sizes are smaller compared to the experimental samples, the trends from our analyses are expected to be generalizable to larger nanoparticles. The dispersion for each nanoparticle is calculated as the ratio of the number of atoms with a coordination number less than 12 (bulk FCC coordination) to the total number of atoms. Further, the d-band center is calculated by evaluating the first moment of the projected density of 5d states for all atoms in the nanoparticle (Equation 3). There is a linear relationship between the d-band center and dispersion (Figure 7e). Additionally, the intercept of linear relation can be interpreted as the d-band center of a bulk Pt atom in the limiting case of zero dispersion.



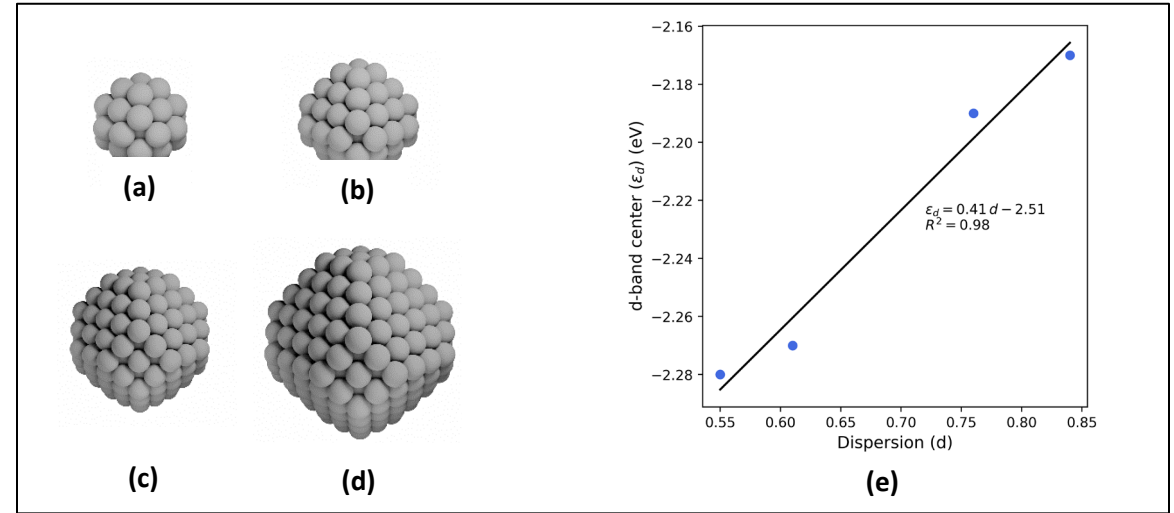


Figure 7. Schematics of octahedral nanoparticle clusters in the order of decreasing dispersion (a) Pt-38, (b) Pt-79, (c) Pt-201, (d) Pt-314. (e) Plot of d-band centers of the nanoparticle clusters against dispersion. A linear fit is also shown along with the slope (0.41), intercept (-2.51 eV), and coefficient of determination ($R^2 = 0.98$).

348 4. Discussion

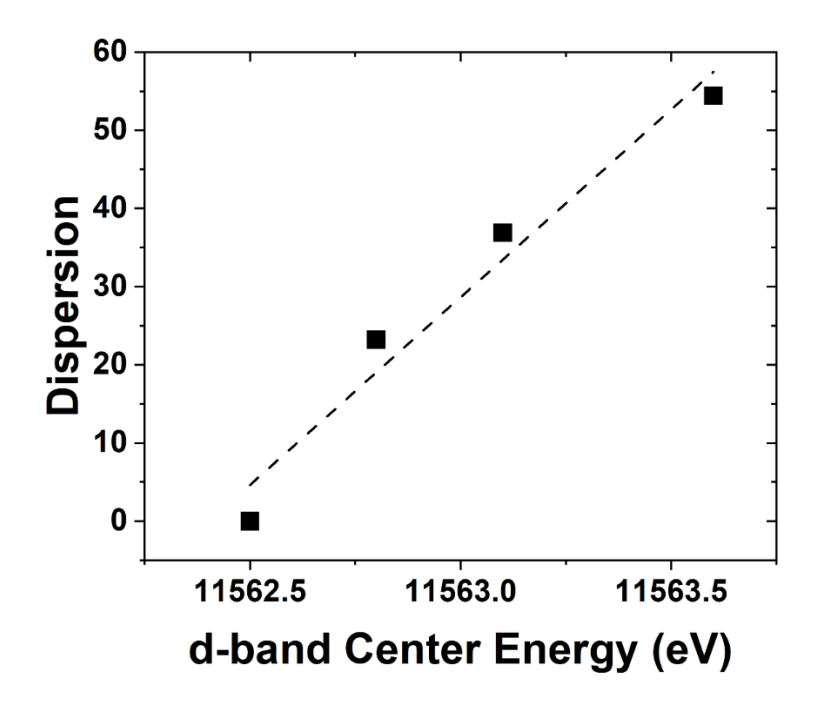


Figure 8. Nanoparticle dispersion versus d-band center energy.

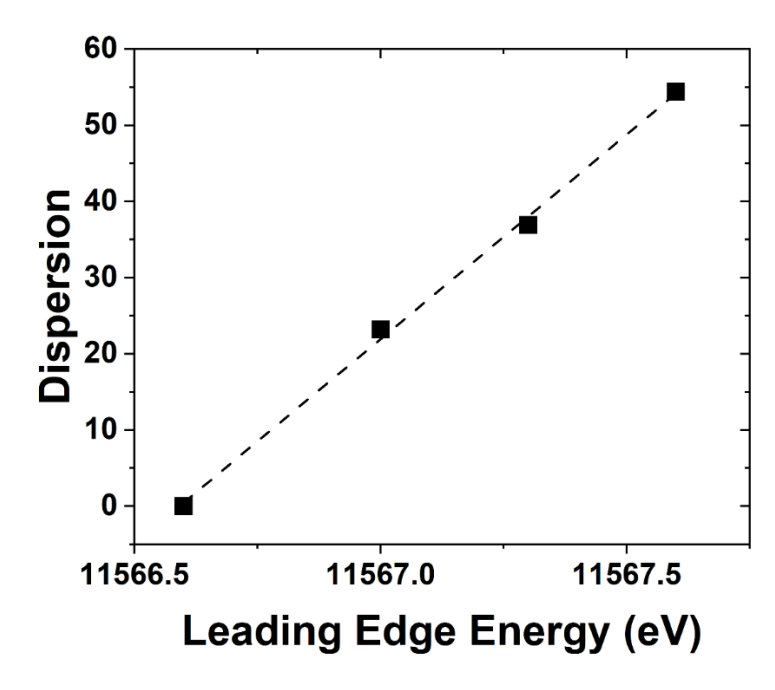


Figure 9. Nanoparticle dispersion versus leading edge energy.

Both the XANES energy shift (Figure 4) and the systematic decrease in FT magnitude of the first three EXAFS oscillations (Figure 3) are characteristic of metallic Pt nanoparticles with decreasing size. ^{8,19} Figure 3 shows a reasonable agreement based on previous literature for metallic Pt nanoparticles and the dispersion determined from EXAFS fitting or STEM. ¹⁰ Therefore, the method used to calculate dispersion is a reasonable estimate for the proportion of fully coordinated (bulk) Pt atoms to undercoordinated (surface) Pt atoms in the nanoparticle samples. Because XANES corresponds with the Pt L_{III} edge, it represents the transition of an electron from a 2p_{3/2} to an unfilled 5d_{3/2} or 5d_{5/2} state, meaning that it can be used to assess properties about the valence electronic structure of Pt. Specifically, it can be used to quantify the average energy of the Pt unfilled 5d states. ^{14,15} Therefore, with decreasing nanoparticle size, the average energy of the unfilled 5d states increases.

Narrowing of the d-DOS has also been observed for similarly sized nanoparticles using high resolution VB-XPS, and the study goes on to attribute the narrowing to the hybridization of fewer wave functions in smaller Pt nanoparticles.²⁰ This could also be due to the narrower nanoparticle size distribution (determined from the STEM imagery). The d-band center shift assessed is also similar to the shift from VB-XPS. Going from nanoparticles of 5.3 nm to 2.4 nm in diameter, there is an increase in d-band center of 0.4 eV for VB-XES.²⁰ In this study, going from nanoparticles 5.1 nm to 2.1 nm in diameter, there is a comparable increase in d-band center of 0.8 eV. Slight differences may be attributed to differences in the oxidation state of each material. While all Pt atoms in this *in-situ* study are metallic (Pt⁰), the Pt atoms in *ex-situ* VB-XES located near the surface of the nanoparticles may be oxidized, leading to a different electronic environment with Pt-O bonds as opposed to only Pt-Pt bonds.^{20,47} The spectra in this study appear broader than the VB-XES spectra. Part of this may be due to the energy resolution of the spectroscopic setup. Other uncertainty may arise from the fact that supported Pt nanoparticles are not all perfectly spherical⁴⁹ and that the number of defects on the surface can differ.

Figure 8 and Figure 9 show the VtC-XES d-band center as well as the energy of the leading edge of the 5d DOS linearly increased with increasing dispersion. There is a strong correlation in both cases, reporting an R-value of 0.981 and 0.999 for the former and the latter respectively. In other words, the proportion of surface atoms to bulk atoms is directly proportional to the shift in the leading-edge energy of the d-DOS. Computationally, similar shifts in the d-band center to higher energy for smaller nanoparticles have been predicted.²¹ A previous study using

computational FEFF modeling for Au nanoparticles of different sizes reports a narrower d band in small Au nanoparticles, with the d-DOS being shifted toward the Fermi level for the smallest nanoparticles.⁴⁵ This study shows a similar trend for Pt, where the spectrum narrows and shifts closer to the Fermi level. Using VB-XPS, similar shifts of the d-band center to higher energy have been observed for nanoparticles of decreasing size. For example, it is reported that for Pt nanoparticles of 5.3 nm and 2.4 nm average diameter, there is a d-band center increase in energy of ~0.4 eV.²⁰ This shift corresponds to the d-band energy increase observed from the large sample to the medium/small samples of between 0.3 and 0.8 eV.

DFT calculations are employed in this study to examine the d-band centers of individual step, terrace, and bulk atoms in Pt-314 to elucidate the cause of the upshift in d-band center with increase in dispersion. In Figure 10a, we plot the d-band centers of a row of bulk atoms along the [100] axis of the nanoparticle capped by terrace atoms on the short (100) facet. The d-band center first shifts downward and then slightly upward on moving from the (100) terrace to the center of the nanoparticle. The d-band center of the center bulk atoms is -2.51 eV, which is equal to the intercept of the linear relationship between d-band center and dispersion. This is consistent with the previous interpretation of the intercept. The overall difference between the d-band center of the terrace atom and the center bulk atom is 0.59 eV. Furthermore, in Figure 10b, the d-band centers of a row of atoms on the (111) terrace capped by step atoms on either side is plotted. The d-band center shifts downward from the step edge to the center of the terrace, with the overall difference equaling 0.15 eV.

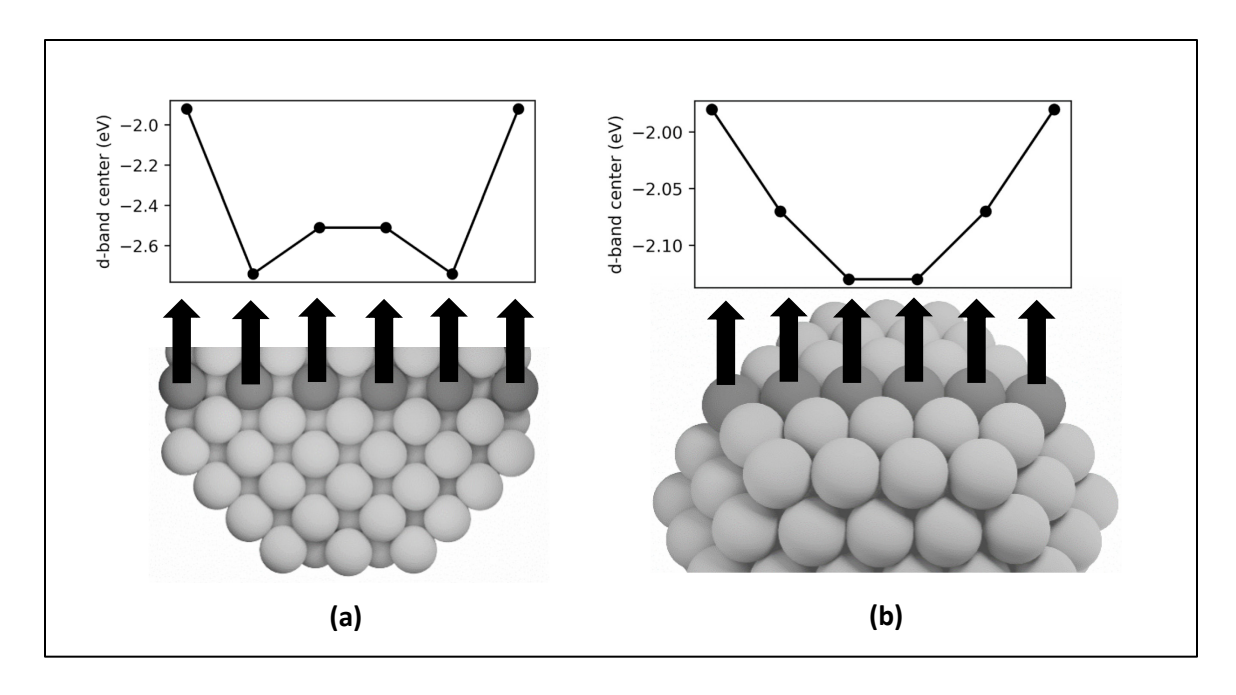


Figure 10. A) Plot of d-band center for each shaded atom along the cross-section of the Pt-314 nanoparticle. The first and last atoms are present on the terraces (CN=9), and the remaining atoms are present in the bulk (CN=12). B) Plot of d-band center for each shaded atom on the terrace of the Pt-314 nanoparticle. The first and last atoms correspond to undercoordinated steps (CN=7) and the remaining atoms correspond to terrace atoms (CN=9).

The downshift in d-band center from the step to the terrace and from the terrace to the bulk can be rationalized on the basis of coordination. Nørskov and coworkers^{54,55} have shown that the d-band center shifts to a lower energy with an increase in the coordination number for single crystal facets of Pt. Moreover, the downshift in d-band center of the subsurface atoms closer to the terrace compared to the center bulk atoms can be explained by the presence of compressive strain at the surface. Many prior studies have shown that strain can lead to shifts in the d-band center, with compressive strain leading to a downshift and tensile strain leading to an upshift.^{54,56-59} Since subsurface atoms have the same coordination as the center bulk atoms, the coordination effect should be negligible. However, since the subsurface atoms have contracted bonds near the surface (see Table S1, Table S2, and Table S3), their d-band center is lower than the bulk atoms. To summarize, since an increase in dispersion corresponds to an increase in the fraction of step and terrace atoms that show higher d-band centers compared to bulk atoms, there is an overall increase in the averaged d-band center of the nanoparticle. The projected density of states is plotted in

Figure 11, which is smoothed using Hanning smoothing as implemented in SciPy.⁵³ The nature of the states transforms from discrete-like to continuous as the nanoparticle size (i.e. the number of atoms) increases.

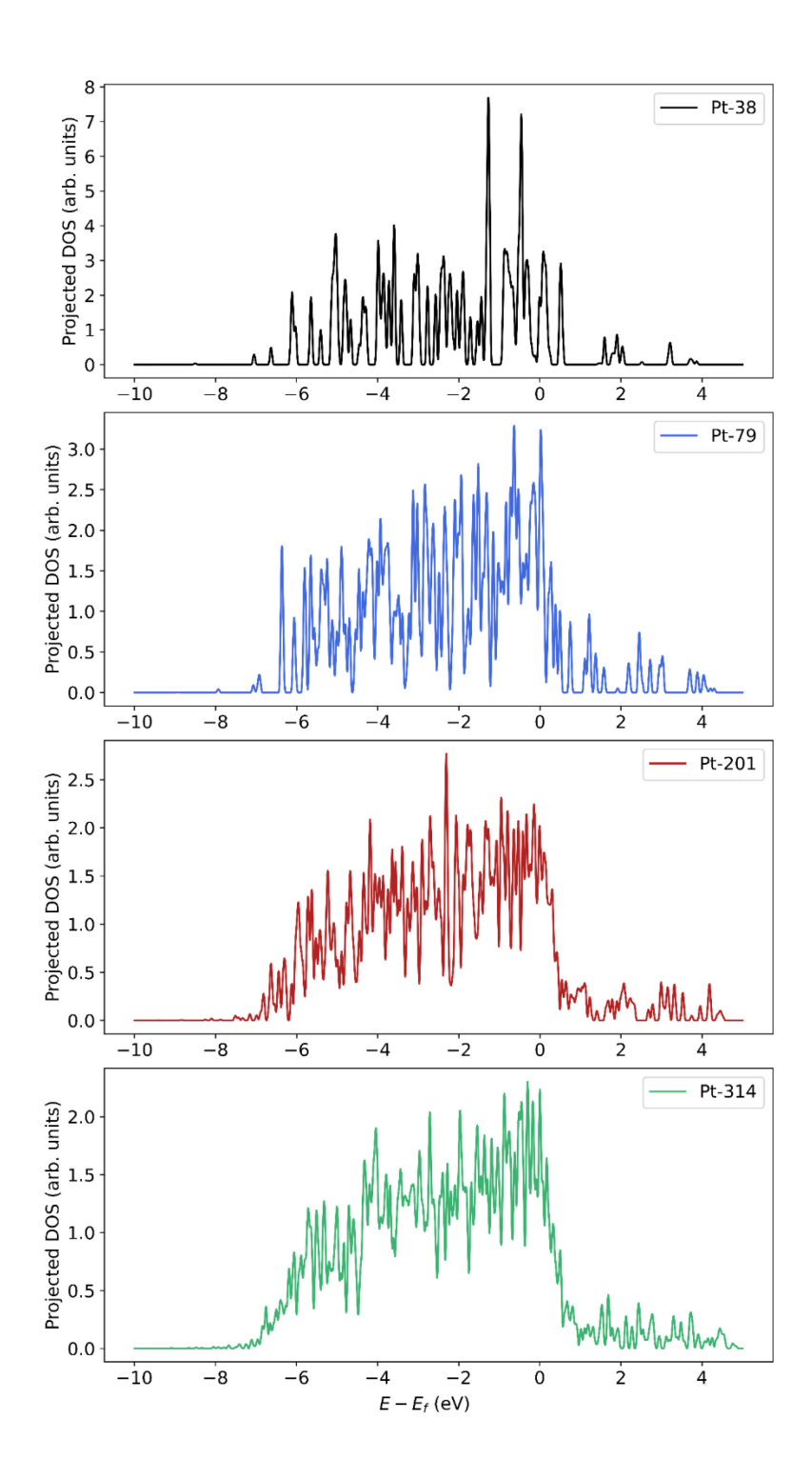


Figure 11. Smoothed projected density of states (pDOS) of Pt atoms in nanoparticles of different sizes. The pDOS is normalized by the number of atoms.

The increase in d-band center energy, which represents the filled Pt 5d states as determined using VtC-XES and DFT, is accompanied by an increase in the average energy of the XANES, which represents the unfilled Pt 5d states. Both the bonding (VtC-XES) and antibonding (XANES) orbitals shift to a higher energy with decreasing nanoparticle size. Changes in the d-DOS are directly related to the catalytic properties of a catalyst material. An increase in the average energy of the filled orbitals may help explain an order of magnitude increase in coking rate for high temperature alkane dehydrogenation with decreasing nanoparticle size. As the energy of the orbitals increases, Pt forms stronger bonds with adsorbates, making it more difficult for species to desorb, which leads to the formation of deeply dehydrogenated species. Just as nanoparticle size can impact selectivity, the size of the nanoparticle can affect the rate of reaction by more than an order of magnitude.

5. Conclusions

This study has synthesized and characterized a series of Pt nanoparticle samples supported on SiO₂ typical of a Pt catalyst material. Using TEM and EXAFS, nanoparticles ranging from 2 nm to 5 nm were quantified with a dispersion ranging from 0% (Pt foil) 50% (small nanoparticle sample). It was found, using VtC-XES at the BNL NSLS-II 8-ID beamline, that the d-band center and leading edge (near - HOMO) density both shift to higher energy with decreasing nanoparticle size. The assessed changes correlate well with the proportion of surface atoms to bulk atoms, pointing to the conclusion that undercoordinated Pt atoms have a different electronic structure than bulk atoms. Differences in the electronic structure may affect rates and selectivity in certain reaction systems by affecting the heat of adsorption/desorption of reactants and products, thereby emphasizing certain pathways or mitigating others. Developments in synchrotron and X-ray detector technology have enabled the resolution of small changes to the d-DOS of Pt atoms in a catalyst material. VtC-XES is a capable technique that is element-specific, can be used for *in-situ* or *in-operando* experiments, and can be used to explain and predict performance of catalyst sites for a variety of reactions. The technique is becoming increasingly available to users at BNL and

across the world, and hopes to enhance catalyst characterization capabilities to obtain unparalleled insights into catalyst materials.

Acknowledgements

This research used resources at the 8-ID Beamline of the National Synchrotron Light Source II, a US Department of Energy Office of Science User Facility operated by Brookhaven National Laboratory under contract no. DE-SC0012704. D.P.D., C.K.R., K.Z., C.W.L., and J.T.M were funded in part by the National Science Foundation (NSF) under Cooperative Agreement No. EEC-1647722. G.S.D. and J.P.G. acknowledge the United States Department of Energy through the Office of Science, Office of Basic Energy Sciences (BES), Chemical, Biological, and Geosciences Division, Data Science Initiative, grant DE-SC0020381. Use of the Center for Nanoscale Materials, U.S. Department of Energy, Office of Science, Office of Basic Energy Sciences User Facility under Contract No. DE-AC02-06CH11357, and of the computational resources from the National Energy Research Scientific Computing Center, is also acknowledged. K.Z. and C.W.L. would like to acknowledge funding from the National Science Foundation grant CHE-2106450.

References

- 1. Filez, M.; Redekop, E. A.; Dendooven, J.; Ramachandran, R. K.; Solano, E.; Olsbye, U.; Weckhuysen, B. M.; Galvita, V. V.; Poelman, H.; Detavernier, C.; Marin, G. B. Formation and functioning of bimetallic nanocatalysts: the power of X-ray probes. *Angew. Chem. Int. Ed.* **2019**, 58, 13220-13230.
- 2. Zimmermann, P.; Peredkov, S.; Abdala, P. M.; DeBeer, S.; Tromp, M.; Müller, C.; van Bokhoven, J. A. Modern X-ray spectroscopy: XAS and XES in the laboratory. *Coord. Chem. Rev.* **2020**, 423, 213466.
- 3. Leshchev, D.; Rakitin, M.; Luvizotto, B.; Kadyrov, R.; Ravel, B.; Attenkofer, K.; Stavitski,
 E. The Inner Shell Spectroscopy beamline at NSLS-II: a facility for in situ and operando
 X-ray absorption spectroscopy for materials research. *J. Synchrotron Rad.* **2022**, 29, 10951106.

- 489 4. Ressler, T. WinXAS: a program for X-ray absorption spectroscopy data analysis under MS-Windows. *J. Synchrotron Radiat.* **1998**, 5, 118-122.
- 5. Glatzel, P.; Sikora, M.; Smolentsev, G.; Fernández-García, M. Hard X-ray photon-in photon-out spectroscopy. *Cat. Today.* **2009**, 145, 294-299.
- 6. Ament, L. J. P.; van Veenendaal, M.; Devereaux, T. P.; Hill, J. P.; van den Brink, J. Resonant inelastic X-ray scattering studies of elementary reactions. *Rev. Mod. Phys.* **2011**, 83, 2, 705-767.
- 7. Singh, J.; Lamberti, C.; van Bokhoven, J. A. Advanced X-ray absorption and emission spectroscopy: in situ catalytic studies. *Chem. Soc. Rev.* **2010**, 39, 4754-4766.
- 8. Lei, Y.; Jelic, J.; Nitsche, L. C.; Meyer, R.; Miller, J. T. Effect of particle size and adsorbates on the L₃, L₂, and L₁ X-ray absorption near edge structure of supported Pt nanoparticles. *Top. Catal.* **2011**, 54, 334-348.
- 9. Schneider, C. A.; Resband, W. S.; Eliceiri, K. W. NIH Image to ImageJ: 25 years of image
 analysis. *Nature Methods*. 2012, 9(7), 671-675.
- 503 10. Miller, J. T.; Kropf, A. J.; Zha, Y.; Regalbuto, J. R.; Delannoy, L.; Louis, C.; Bus, E.; van 504 Bokhoven, J. A. The effect of gold particle size on Au-Au bond length and reactivity 505 toward oxygen in supported catalysts. *J. Catal.* **2006**, 240, 222-234.
- 11. Vollath, D. (2013) Nanoparticles-nanocomposites-nanomaterials: an introduction for
 beginners. Wiley-VCH Verlag GmbH & Co. Weinheim, Germany.
- 12. Pryadchenko, V. V.; Srabionyan, V. V.; Avakyan, L. A.; van Bokhoven, J. A.; Bugaev, L.
 A. Electronic structure of Pt and Au compounds measured by X-ray emission and X-ray absorption spectroscopy. *J. Phys. Chem. C.* 2012, 116, 25790-25796.
- 13. Hammer, B.; Nørskov, J. K. Electronic factors determining the reactivity of metal surfaces.
 Surf. Sci. 1995, 343, 211-220.
- 14. Purdy, S. C.; Ghanekar, P.; Mitchell, G.; Kropf, A. J.; Zemlyanov, D. Y.; Ren, Y.; Riveiro,
 F.; Delgass, W. N.; Greeley, J.; Miller, J. T. Origin of electronic modification of platinum
 in a Pt₃V alloy and its consequences for propane dehydrogenation catalysis. *ACS Appl. Energy Mater.* 2020, 3, 1410-1422.
- 15. Cybulskis, V. J.; Bukowski, B. C.; Tseng, H.; Gallagher, J. R.; Wu, Z.; Wegener, E.; Kropf,
 A. J.; Ravel, B.; Ribeiro, F. H.; Greeley, J.; Miller, J. T. Zinc promotion of platinum for

- 519 catalytic light alkane dehydrogenation: insights into geometric and electronic effects. *ACS*520 *Catal.* **2017**, 7, 4173-4181.
- 521 16. Kittel, C. (2004) *Introduction to solid state physics* (8th ed.). John Wiley & Sons.
- 17. Yang, M.; Zhu, Y.; Zhou, X.; Sui, Z.; Chen, D. First-principles calculations of propane dehydrogenation over PtSn catalysts. *ACS Catal.* **2012**, 2, 1247-1258.
- 18. Smith, N. V.; Wertheim, G. K.; Hüfner, S.; Traum, M. M. Photoemission spectra and band structures of d-band metals. IV. X-ray photoemission spectra and densities of states in Rh, Pd, Ag, Ir, Pt, and Au.
- 19. Behafarid, F.; Ono, L. K.; Mostafa, S.; Croy, J. R.; Shafai, G.; Hong, S.; Rahman, T. S.;
 Bare, S. R.; Cuenya, B. R. Electronic properties and charge transfer phenomena in Pt
 nanoparticles on γ-Al₂O₃: size, shape, support, and adsorbate effects.
- 530 20. Bai, L.; Wang, X.; Chen, Q.; Ye, Y.; Zheng, H.; Guo, J.; Yin, Y.; Gao, C. Explaining the 531 size dependence in Platinum-nanoparticle-catalyzed hydrogenation reactions. *Angew*. 532 *Chem. Int. Ed.* **2016**, 55, 15656-15661.
- 21. Sun, Y.; Zhuang, L.; Lu, J.; Hong, X.; Liu, P. Collapse in crystalline structure and decline
 in catalytic activity of Pt nanoparticles on reducing particle size to 1 nm. *J. Am. Chem. Soc.* 2007, 129, 15465-15467.
- 536 22. Glatzel, P.; Bergmann, U. High resolution 1s core hole X-ray spectroscopy in 3d transition
 537 metal complexes electronic and structural information. *Coord. Chem. Rev.* 2005, 249,
 538 65-95.
- 23. Kim, J.; Casa, D.; Upton, M. H.; Gog, T.; Kim, Y.; Mitchell, J. F.; van Veenendaal, M.;
 Daghofer, M.; van den Brink, J.; Khaliullin, G.; Kim, B. J. Magnetic excitation spectra of
 Sr₂IrO₄ probed by resonant inelastic X-ray scattering: establishing links to cuprate
 superconductors. *Phys. Rev. Lett.* 2012, 108, 177003.
- 543 24. Glatzel, P.; Singh, J.; Kvashnina, K. O.; van Bokhoven, J. A. In situ characterization of the 544 5d density of states of Pt nanoparticles upon adsorption of CO. *J. Am. Chem. Soc.* **2010**, 545 132, 2555-2557.
- 546 25. Wegener, E. C.; Bukowski, B. C.; Yang, D.; Wu, Z.; Kropf, A. J.; Delgass, W. N.; Greeley, J.; Zhang, G.; Miller, J. T. Intermetallic compounds as an alternative to single-atom alloy catalysts: geometric and electronic structures from advanced X-ray spectroscopies and computational studies. *ChemCatChem*, **2020**, 12, 1325-1333.

- 26. Kobayashi, K. Hard X-ray photoemission spectroscopy. *Nucl. Instrum. Methods Phys. Res* 2009, 601, 32-47.
- 552 27. Smolentsev, G.; Soldatov, A. V.; Messinger, J.; Merz, K.; Weyhermüller, T.; Bergmann,
- 553 U.; Pushkar, Y.; Yano, J.; Yachandra, V. K.; Glatzel, P. X-ray emission spectroscopy to
- study ligand valence orbitals in Mn coordination complexes. *J. Am. Chem. Soc.* **2009**, 131,
- 555 13161-13167.
- 556 28. Bauer, M. HERFD-XAS and valence-to-core-XES: new tools to push the limits in research with hard X-rays? *Phys. Chem. Chem. Phys.* **2014**, 16, 13827-13837.
- 558 29. Pollock, C. J.; DeBeer, S. Valence-to-core X-ray emission spectroscopy: a sensitive probe 559 of the nature of a bound ligand. *J. Am. Chem. Soc.* **2011**, 133, 5594-5601.
- 30. Boubnov, A.; Carvalho, H. W. P.; Doronkin, D. E.; Günter, T.; Gallo, E.; Atkins, A. J.; Jacob, C. R.; Grunwaldt, J. Selective catalytic reduction of NO over Fe-ZSM-5: mechanistic insights by operando HERFD-XANES and valence-to-core X-ray emission
- spectroscopy. J. Am. Chem. Soc. **2014**, 136, 37, 13006-13015.
- 31. Safonov, V. A.; Vykhodtseva, L. N.; Polukarov, Y. M.; Safonova, O. V.; Smolentsev, G.;
- Sikora, M.; Eeckhout, S. G.; Glatzel, P. Valence-to-core X-ray emission spectroscopy
- identification of carbide compounds in nanocrystalline Cr coatings deposited from Cr(III)
- electrolytes containing organic substances. *J. Phys. Chem. B* **2006**, 110, 23192-23196.
- 32. Kopelent, R.; van Bokhoven, J. A.; Nachtegaal, M.; Szlachetko, J.; Safonova, O. V. X-ray
- emission spectroscopy: highly sensitive techniques for time-resolved probing of cerium
- reactivity under catalytic conditions. *Phys. Chem. Chem. Phys.* **2016**, 18, 32486.
- 33. Bayindir, Z.; Duchesne, P. N.; Cook, S. C.; MacDonald, M. A.; Zhang, P. X-ray
- spectroscopy studies on the surface structural characteristics and electronic properties of
- platinum nanoparticles. *J. Chem. Phys.* **2009**, 131, 244716.
- 34. Chen, J.; Finfrock, Y. Z.; Wang, Z.; Sham, T. Strain and ligand effects in Pt-Ni alloys
- studies by valence-to-core X-ray emission spectroscopy. Sci. Rep 2021, 11, 13698.
- 35. Geoghegan, B. L., Liu, Y., Peredkov, S., Dechert, S., Meyer, F., DeBeer, S., Cutsail III, G.
- E. Combining valence-to-core X-ray emission and Cu K-edge X-ray absorption
- spectroscopies to experimentally assess oxidation state of organometallic Cu(I)/(II)/(III)
- 579 complexes. J. Am. Chem. Soc. **2022**, 144, 2520-2534.

- 36. Giordanino, F., Borfecchia, E., Lomachenko, K., Lazzarini, A., Agostini, G., Gallo, E.,
- Soldatov, A., Beato, P., Bordiga, S., Lamberti, C. Interaction of NH3 with Cu-SSZ-13
- catalyst: a complementary FTIR, XANES, and XES study. J. Phys. Chem. Lett. 2014, 5,
- 583 1552-1559.
- 37. Sattler, J. J. H. B.; Ruiz-Martinez, J.; Santillan-Jimenez, E.; Weckhuysen, B. M. Catalytic
- dehydrogenation of light alkanes on metals and metal oxides. Chem. Rev. 2014, 114,
- 586 10613-10653.
- 38. Marković, N. M.; Schmidt, T. J.; Stamenković, V.; Ross, P. N. Oxygen reduction reaction
- on Pt and Pt bimetallic surfaces: a selective review. *Fuel Cells*, **2001**, 1, 2, 105-116.
- 39. Garino, C.; Borfecchia, E.; Gobetto, R.; van Bokhoven, J. A.; Lamberti, C. Determination
- of the electronic and structural configuration of coordination compounds by synherotron-
- radiation techniques. *Coord. Chem. Rev.* **2014**, 277-278, 130-186.
- 40. Zhu, J.; Yang, M.; Yu, Y.; Zhu, Y.; Sui, Z.; Zhou, X.; Holmen, A.; Chen, D. Size-dependent
- reaction mechanism and kinetics for propane dehydrogenation over Pt catalysts. ACS
- 594 *Catal.* **2015**, 5, 6310-6319.
- 595 41. Zhou, Y.; Doronkin, D. E.; Chen, M.; Wei, S.; Grunwaldt, J. Interplay of Pt and crystal
- facets of TiO₂: CO oxidation activity and *operando* XAS/DRIFTS studies. ACS Catal.
- **2016**, 6, 7799-7809.
- 42. Ravel, B.; Kropf, A. J.; Yang, D.; Wang, M.; Topsakal, M.; Lu, D.; Stennett, M. C.; Hyatt,
- N. C. Nonresonant valence-to-core X-ray emission spectroscopy of niobium. *Phys. Rev. B*
- **2018**, 97, 125139.
- 43. Garino, C.; Gallo, E.; Smolentsev, N.; Glatzel, P.; Gobetto, R.; Lamberti, C.; Sadler, P. J.;
- Salassa, L. Resonant X-ray emission spectroscopy reveals d-d ligand-field states involved
- in the self-assembly of a square-planar platinum complex. *Phys. Chem. Chem. Phys.* **2012**,
- 604 14, 15278-15281.
- 44. Kaya, S.; Friebel, D.; Ogasawara, H.; Anniyev, T.; Nilsson, A. Electronic structure effects
- in catalysis probed by X-ray and electron spectroscopy. J. Electron Spectros. Relat.
- 607 *Phenomena.* **2013**, 190, 113-124.
- 45. Van Bokhoven, J. A.; Miller, J. T. d electron density and reactivity of the d band as a
- function of particle size in supported gold catalysts. *J. Phys. Chem. C* **2007**, 9245-9249.

- 46. Hammer, B.; Nørskov, J. K. Theoretical surface science and catalysis calculations and
 concepts. Adv. Catal 2000, 45, 71-129.
- 47. LiBretto, N. J.; Yang, C.; Ren, Y.; Zhang, G.; Miller, J. T. Identification of surface structures in Pt₃Cr intermetallic nanocatalysts. *Chem. Mater.* **2019**, 1597-1609.
- 48. Singh, J.; Nelson, R. C.; Vicente, B. C.; Scott, S. L.; van Bokhoven, J. A. Electronic structure of alumina-supported monometallic Pt and bimetallic PtSn catalysts under hydrogen and carbon monoxide environment. *Phys. Chem. Chem. Phys.* **2010**, 12, 5668-5677.
- 49. Simonsen, S. B.; Chorkendorff, I.; Dahl, S.; Skoglundh, M.; Meinander, K.; Jensen, T. N.;
 Lauritsen, J. V.; Helveg, S. Effect of particle morphology on the ripening of supported Pt
 nanoparticles. J. Phys. Chem. C 2012, 116, 9, 5646-5653.
- 50. Larsen, H. A.; Mortensen, J. J.; Blomqvist, J.; Castelli, I. E.; Christensen, R.; Dułak, M.; Friis, J.; Groves, M. N.; Hammer, B.; Hargus, C.; Hermes, E. D.; Jennings, P. C.; Jensen,
- P. B.; Kermode, J.; Kitchin, J. R.; Kolsbjerg, E. L.; Kubal, J.; Kaasbjerg, K.; Lysgaard, S.;
- Maronsson, J. B.; Maxson, T.; Olsen, T.; Pastewka, L.; Peterson, A.; Rostgaard, C.;
- Schiøtz, J.; Schütt, O.; Strange, M.; Thygesen, K. S.; Vegge, T.; Vilhelmsen, L.; Walter,
- M.; Zeng, Z.; Jacobsen, K. W. The atomic simulation environment a Python library for working with atoms. *J. Phys.: Condens. Matter* **2017**, 29, 273002.
- 51. Kresse, G.; Furthmü, J. Efficient iterative schemes for ab initio total-energy calculations using a plane-wave basis set. *Phys. Rev. B* **1996**, 54, 16, 11169-11186.
- 52. Blöchl, P. E. Projector augmented-wave method. *Phys. Rev. B* **1994**, 50, 17953.
- 53. Virtanen, P.; Gommers, R.; Oliphant, T. E.; Haberland, M.; Reddy, T.; Cournapeau, D.;
- Burovski, E.; Peterson, P.; Weckesser, W.; Bright, J.; van der Walt, S. J.; Brett, M.; Wilson,
- J.; Millman, K. J.; Mayorov, N.; Nelson, A. R. J.; Jones, E.; Kern, R.; Larson, E.; Carey,
- 634 C. J.; Polat, İ.; Feng, Y.; Moore, E. W.; VanderPlas, J.; Laxalde, D.; Perktold, J.; Cimrman,
- R.; Henriksen, I.; Quintero, E. A.; Harris, C. R.; Archibald, A. M.; Ribeiro, A. H.;
- Pedregosa, F.; van Mulbregt, P.; Vijaykumar, A.; Bardelli, A. Pietro; Rothberg, A.; Hilboll,
- A.; Kloeckner, A.; Scopatz, A.; Lee, A.; Rokem, A.; Woods, C. N.; Fulton, C.; Masson,
- 638 C.; Häggström, C.; Fitzgerald, C.; Nicholson, D. A.; Hagen, D. R.; Pasechnik, D. V.;
- Olivetti, E.; Martin, E.; Wieser, E.; Silva, F.; Lenders, F.; Wilhelm, F.; Young, G.; Price,
- G. A.; Ingold, G. L.; Allen, G. E.; Lee, G. R.; Audren, H.; Probst, I.; Dietrich, J. P.; Silterra,

- J.; Webber, J. T.; Slavič, J.; Nothman, J.; Buchner, J.; Kulick, J.; Schönberger, J. L.; de
- Miranda Cardoso, J. V.; Reimer, J.; Harrington, J.; Rodríguez, J. L. C.; Nunez-Iglesias, J.;
- Kuczynski, J.; Tritz, K.; Thoma, M.; Newville, M.; Kümmerer, M.; Bolingbroke, M.;
- Tartre, M.; Pak, M.; Smith, N. J.; Nowaczyk, N.; Shebanov, N.; Pavlyk, O.; Brodtkorb, P.
- A.; Lee, P.; McGibbon, R. T.; Feldbauer, R.; Lewis, S.; Tygier, S.; Sievert, S.; Vigna, S.;
- Peterson, S.; More, S.; Pudlik, T.; Oshima, T.; Pingel, T. J.; Robitaille, T. P.; Spura, T.;
- Jones, T. R.; Cera, T.; Leslie, T.; Zito, T.; Krauss, T.; Upadhyay, U.; Halchenko, Y. O.;
- Vázquez-Baeza, Y. SciPy 1.0: fundamental algorithms for scientific computing in Python.
- *Nat. Methods* **2020**, 17, 261-272.
- 54. Mavrikakis, M.; Hammer, B.; Nørskov, J. K. Effect of strain on the reactivity of metal
- 651 surfaces. Phys. Rev. Lett. 1998, 81, 2819.
- 55. Jiang, T.; Mowbray, D. J.; Dobrin, S.; Falsig, H.; Hvolbæk, B.; Bligaard, T.; Nørskov, J.
- K. Trends in CO oxidation rates for metal nanoparticles and close-packed, stepped, and
- kinked surfaces. J. Phys. Chem. C 2009, 113, 24, 10548-10553.
- 56. Wang, L.; Zeng, Z.; Gao, W.; Maxson, T.; Raciti, D.; Giroux, M.; Pan, X.; Wang, C.;
- Greeley, J. P. Tunable intrinsic strain in two-dimensional transition metal electrocatalysts.
- 657 Science **2019**, 363, 6429, 870-874.
- 57. Kitchin, J. R.; Nørskov, J. K.; Barteau, M. A.; Chen, J. G. Role of strain and ligand effects
- in the modification of the electronic and chemical properties of bimetallic surfaces. *Phys.*
- 660 Rev. Lett. 2004, 93, 156801.
- 58. Abild-Pedersen, F.; Greeley, J. P.; Nørskov, J. K. Understanding the effect of steps, strain,
- poisons, and alloying: methane activation on Ni surfaces. Catalysis Letters 2005, 105, 9-
- 663 13.
- 59. Strasser, P.; Koh, S.; Anniyev, T.; Greeley, J. P.; More, K.; Yu, C.; Liu, Z.; Kaya, S.;
- Nordlund, D.; Ogasawara, H.; Toney, M. F.; Nilsson, A. Lattice-strain control of the
- activity in dealloyed core-shell fuel cell catalysts. *Nature Chemistry* **2010**, 2, 454-460.
- 60. Alcala, R.; Dean, D. P.; Chavan, I.; Chang, C.; Burnside, B.; Pham, H. N.; Peterson, E.;
- Miller, J. T.; Datye, A. K. Strategies for regeneration of Pt-alloy catalysts supported on
- silica for propane dehydrogenation. *Appl. Cat. A: Gen.* **2023**, 658, 119157.

Supporting Information

The lattice strain for surface, subsurface, and bulk atoms of Pt-314 is calculated. The x-, y-, and z-components of strain for the surface, subsurface, and bulk atoms of Pt (designed in the nanoparticle in **Figure S1**) are calculated and tabulated in **Table S1**, **Table S2**, and **Table S3**.

The strain (ϵ_{ij}) for a bond between two atoms having a bond length of a_{ij} in a lattice with a lattice constant of a_{Pt} is calculated as follows:

$$\epsilon_{ij} = \frac{a_{ij} - a_{Pt}}{a_{Pt}}$$

The components of strain are calculated as follows:

$$\epsilon_{ij}^{x} = \epsilon_{ij} \left(\cos(\theta_{xy}) + \sin(\theta_{xz}) \right)$$

$$\epsilon_{ij}^{y} = \epsilon_{ij} (\sin(\theta_{xy}) + \cos(\theta_{yz}))$$

$$\epsilon_{ij}^{z} = \epsilon_{ij} \left(\cos(\theta_{xz}) + \sin(\theta_{yz}) \right)$$

683 Where θ_{xy} , θ_{yz} , θ_{xz} represent the angles made by the bonds with the x-axis (in the xy plane), y-684 axis (in the yz-plane), z-axis (in the xz-plane) respectively.

From the tabulated values of strain, it is evident that the sub-surface atom experiences an unusually large magnitude of compressive strain (~47%) in the axial (or x-) direction, which neither the surface nor the bulk atom experience.

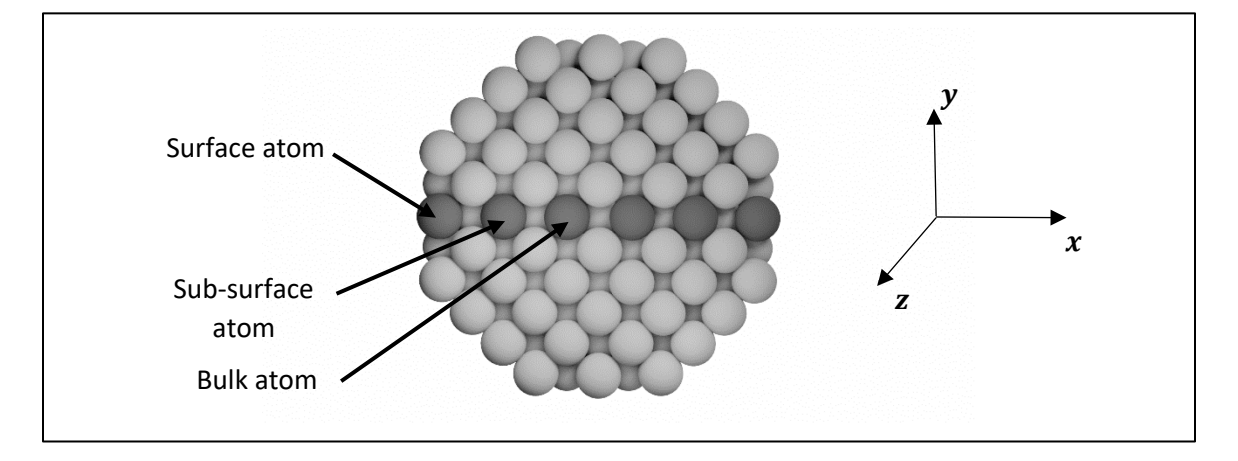


685

686

687

672



689

690

691

Figure S1: Cross section of the Pt-314 nanoparticle with the surface, sub-surface, and bulk atoms annotated.

Table S1: Bond lengths and angles for bonds of the surface atom with its 8 neighbors and calculated strains.

	$a_{ij}(ext{Å})$	$\theta_{xy}(^{\circ})$	$oldsymbol{ heta_{yz}}(^{\circ})$	$\boldsymbol{ heta_{xz}}(^{\circ})$	ϵ_{ij}	ϵ^x_{ij}	ϵ_{ij}^{y}	$\epsilon_{ij}^{\mathrm{z}}$
	2.75	90.0	45.0	0.0	-0.024	0.000	-0.041	-0.016
	2.75	90.0	45.0	0.0	-0.024	0.000	-0.041	-0.016
	2.75	90.0	45.0	0.0	-0.024	0.000	-0.041	-0.016
Surface	2.75	90.0	45.0	0.0	-0.024	0.000	-0.041	-0.016
atom	2.83	0.0	90.0	45.7	0.001	0.002	0.000	0.001
	2.83	0.0	90.0	45.7	0.001	0.002	0.001	0.001
	2.83	44.3	0.0	90.0	0.001	0.002	0.002	0.000
	2.83	44.3	0.0	90.0	0.001	0.002	0.001	0.000
	Net strain							-0.062

Table 2: Bond lengths and angles for bonds of the sub-surface atom with its 12 neighbors and calculated strains.

	$a_{ij}(ext{Å})$	$\theta_{xy}(^{\circ})$	$\boldsymbol{\theta}_{yz}(^{\circ})$	$ heta_{xz}(^{\circ})$	ϵ_{ij}	ϵ^{x}_{ij}	ϵ_{ij}^{y}	ϵ_{ij}^z
	2.89	90.0	45.0	0.0	0.025	0.000	0.042	0.018
	2.89	90.0	45.0	0.0	0.025	0.000	0.042	0.018
Sub-	2.89	90.0	45.0	0.0	0.025	0.000	0.042	0.018
Surface	2.89	90.0	45.0	0.0	0.025	0.000	0.042	0.018
atom	2.76	0.0	90.0	43.8	-0.023	-0.039	0.000	-0.023
	2.76	0.0	90.0	43.8	-0.023	-0.039	0.000	-0.023
	2.69	0.0	90.0	42.8	-0.047	-0.079	0.000	-0.047

	2.69	0.0	90.0	42.8	-0.047	-0.079	0.000	-0.047
	2.69	47.2	0.0	90.0	-0.047	-0.079	-0.081	0.000
	2.69	47.2	0.0	90.0	-0.047	-0.079	-0.081	0.000
	2.76	46.2	0.0	90.0	-0.023	-0.039	-0.040	0.000
	2.76	46.2	0.0	90.0	-0.023	-0.039	-0.040	0.000
Net strain							-0.074	-0.068

Table S3: Bond lengths and angles for bonds of the bulk atom with its 12 neighbors and calculated strains.

	$a_{ij}(ext{Å})$	$\theta_{xy}(^{\circ})$	$ heta_{yz}(^{\circ})$	$\theta_{xz}(^{\circ})$	ϵ_{ij}	ϵ^x_{ij}	ϵ_{ij}^{y}	ϵ^z_{ij}
	2.79	90.0	45.0	0.0	-0.010	0.000	-0.017	-0.007
	2.79	90.0	45.0	0.0	-0.010	0.000	-0.017	-0.007
	2.79	90.0	45.0	0.0	-0.010	0.000	-0.017	-0.007
	2.79	90.0	45.0	0.0	-0.010	0.000	-0.017	-0.007
	2.82	0.0	90.0	45.0	0.000	0.000	0.000	0.000
Bulk	2.82	0.0	90.0	45.0	0.000	0.000	0.000	0.000
atom	2.79	0.0	90.0	44.5	-0.011	-0.019	0.000	-0.011
	2.79	0.0	90.0	44.5	-0.011	-0.019	0.000	-0.011
	2.82	45.0	0.0	90.0	0.000	0.000	0.000	0.000
	2.82	45.0	0.0	90.0	0.000	0.000	0.000	0.000
	2.79	45.5	0.0	90.0	-0.011	-0.019	-0.019	0.000
	2.79	45.5	0.0	90.0	-0.011	-0.019	-0.019	0.000
	Net strain							-0.050